LATERAL BLOWING IMPACT ON CORNER VORTEX SHEDDING IN SOLID ROCKET MOTORS

SPACE PROPULSION 2016
MARRIOTT PARK HOTEL, ROME, ITALY / 2-6 MAY 2016

Laura Lacassagne(1)(2), Thibault Bridel-Bertomeu(1)(3), Eleonore Riber(1), Benedicte Cuenot(1), Gregoire Casalis(4), Franck Nicoud(5),

(1) CERFACS, 31057 Toulouse, France, Emails: lacassa@cerfacs.fr, tbridel@cerfacs.fr, riber@cerfacs.fr, cuenot@cerfacs.fr
(2) Herakles, Rue de Touban - Les Cinq Chemins 33185 Le Haillan France
(3) CNES/DLA - Rue Jacques Hillairet, 75612 Paris, France
(4) ONERA, Toulouse 31055, France, Email: gregoire.casalis@onera.fr
(5) University of Montpellier, 34095 Montpellier Cedex, France, Email: franck.nicoud@umontpellier.fr

KEYWORDS: Corner vortex shedding, solid rocket motors, large eddy simulation, linear stability

ABSTRACT:

The corner vortex shedding in solid rocket motors also called VSA is studied in an academic configuration with compressible unsteady simulation and linear stability analysis. Lateral blowing impact on the stability of the flow is analysed thanks to parametric unsteady simulations by varying the flow rate over the upper surface. The results clearly show a stabilization of the flow when lateral blowing increases. Linear stability analysis on local velocity profiles enables to accurately reconstruct the mode on a selected weakly unstable case, although the frequency selection mechanism is not well captured. The same analysis is performed on a stable case and even if strong differences are noticed, linear stability do not give a conclusion as clear as the one obtained with numerical simulations. More generally, these results show a stabilization effect of the lateral blowing on corner vortex shedding and the ability of the linear stability analysis to reproduce and predict this mechanism.

1. INTRODUCTION

Pressure oscillations are a major issue in solid rocket motors (SRM) and designing motors that produce as small pressure oscillations as possible represents an important industrial challenge.

For about 30 years, several studies have been devoted to understand and characterize instability mechanisms that trigger pressure oscillations.

Starting from the experimental observation that the internal pressure oscillation frequencies are close to the frequencies of the longitudinal acoustic modes, one of the first method to analyse motor stability, introduced by Majdalani and Flandro was based on acoustics balance [29], [21]. However, considering only acoustic appears to be insufficient to explain the emergence of pressure oscillations having frequencies that evolve in time [20].

Following pioneer works [38, 7, 19, 21], sources of internal pressure fluctuations have been intensively studied, especially in France [9, 36, 12, 3] in the context of the Ariane 5 launcher. Vortex shedding induced by hydrodynamic instabilities appears as a possible source of pressure oscillation and as proposed by Vuillot [39], three triggering mechanisms can be identified: vortex shedding induced by an obstacle, by a corner and a wall. This latter mechanism called parietal vortex shedding and induced by an intrinsic instability of the flow has been the subject of extensive theoretical studies [9, 24, 22, 23, 14, 6, 15, 28] based on linear stability of the simplified Taylor-Culick flow model [35, 17]. The good comparison of this approach with pressure oscillations observed in subscale [13] and in a real full scale motor [4] have definitively put this intrinsic flow instability as a proven source of pressure fluctuations and the knowledge acquired enables to understand and predict correctly this mechanism.

In the context of monolithic configurations, the Corner Vortex Shedding, CVS also referred as VSA [39] appears as a potential source of instability. This instability can be generated when geometry exhibits a propellant chamfered edge generating strong shear flow in the cross-stream direction. Shear flows are known to be prone to instabilities since temporally or spatially growing waves are generated along the stream and lead to the formation of unsteady vortices. In the past 50 years, stability of shear layers has been continuously studied and the stability theory is today well established [18], [25], [34]. However, because of headwall injections which are characteristic of SRMs flows, velocity profiles generated in the shear layer are quite different from the ones of simple hyperbolic-tangent mixing layers [30], [31]. The study of this particular mixing layer is needed to better predict and understand CVS.

This work aims at performing unsteady simulations of lateral blowing on a SRM shear layer. In order to focus on CVS, the simulations are performed in an academic configuration taking into

account only the shear region in a two dimensional axisymmetric geometry. This configuration is however representative in terms of dimensions, velocity profiles, temperature and pressure of a real motor.
This paper is organized as follows. First of all the studied configuration and operating point are defined. Then, after a quick presentation of the unsteady simulation solver, the results of the parametric study are presented showing stabilisation of the mixing layer by lateral blowing. Elements of linear stability theory are recalled in section 5, followed by the analysis of an unstable case in section 6. This study focuses first on one axial position and then the 2D axial velocity perturbation is reconstructed and compared to the unsteady simulation results. Finally the same analysis is performed on a stable case for qualitative comparison and conclusion purposes.

2. CONFIGURATION

The geometry for the present study was chosen to reproduce and isolate the CVS instability as it can be found in a solid rocket motor.

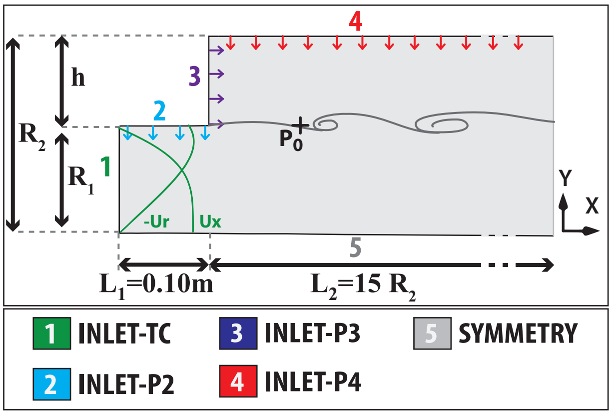

Figure 1. Schematic view of the configuration

As shown in Fig. 1, the geometry is a 2D axisymmetric configuration composed of a cylinder with injecting headwalls at an injection speed V_{inj} of 10.2 m/s. This unrealistic injection velocity is chosen to optimise computational time. Moreover same results have been observed with an injection velocity 10 times smaller. The driving parameter of the instability is the velocity ratio between the upper and the lower part of the mixing layer. The channel includes a sharp section change with a step height h equals to 0.115 m. The inlet radius R_1 and the outlet radius R_2 are respectively equal to 0.135 m and 0.25 m. The output of the domain is located at $15.R_2$ away from the corner. To reduce the computational domain, the well known Taylor-Culick profile [35], [17], representative of flow induced by headwall injection, is imposed over the boundary condition noted *INLET-TC* on Fig. 1. Velocity profiles are set to represent a 0.25 m long headwall injection channel. Operating point parameters are summarized in Tab.1.

General parameters			
Temperature	T	3500	K
Pressure	P	50	$bars$
Propellant mass flow rate	Q	50.82	$kg/s/m^2$
Propellant gas parameters			
Molar mass	M	2.97×10^{-2}	kg/mol
Reference temperature	T_0	2324	K
Reference viscosity	μ_0	7.2×10^{-5}	$kg/m/s$
Heat capacity	C_{pg}	2057	$J/kg.K$

Table 1. Operating point parameters

The mesh is composed of about 2.6 million triangles. A quasi-constant space discretization of $\Delta x = 2.0.10^{-4}$ m is applied from the upstream inlet to a distance of $3.R_2$ away from the corner. Then the mesh is coarsened down to the outlet. Around 600 points are in the inlet radius R_1 and about 13 points in the shear layer.

3. THE UNSTEADY SIMULATION SOLVER

The unsteady simulations were performed with the code AVBP [1], jointly developed by CERFACS and IFPEN. AVBP, based on a cell-vertex finite volume formulation, solves the fully compressible Navier-Stokes equations on unstructured hybrid grids. The main convective schemes are a finite-volume Lax-Wendroff type scheme (LW) and finite-element two-step Taylor-Galerkin scheme (TTGC) [16]. These two schemes are respectively 2^{nd} and 3^{rd} order in time and space. The diffusive scheme is a typical 2^{nd} order compact scheme.
The simulations presented in this paper are performed with the 2^{nd} order convective scheme.

4. MODIFICATION OF THE FLOW FIELD

Parametric unsteady simulations were performed with only one varying parameter, the mass flow rate Q_{P4} imposed over the upper boundary condition noted *INLET-P4* on Fig. 1. Mass flow rate Q_{P2} and Q_{P3} over surfaces *INLET-P2* and *INLET-P3* respectively are constant and equal to $Q = 50.82$ kg/m/s as referred in Tab. 1.
Starting from the nominal condition called *R100* in Tab. 2, where Q_{P4} is equal to $Q = 50.82$ kg/m/s, Q_{P4} is decreased by steps of 10% until the case *R000* where no gas is injected through the surface.
The simulated cases with the corresponding values of Q_{P4} are summarized in Tab. 2.
The blowing impact can be qualitatively visualized by vorticity fields in the axial plane presented for the several blowing intensities on Fig. 2.
Theses results clearly show the stabilization of the

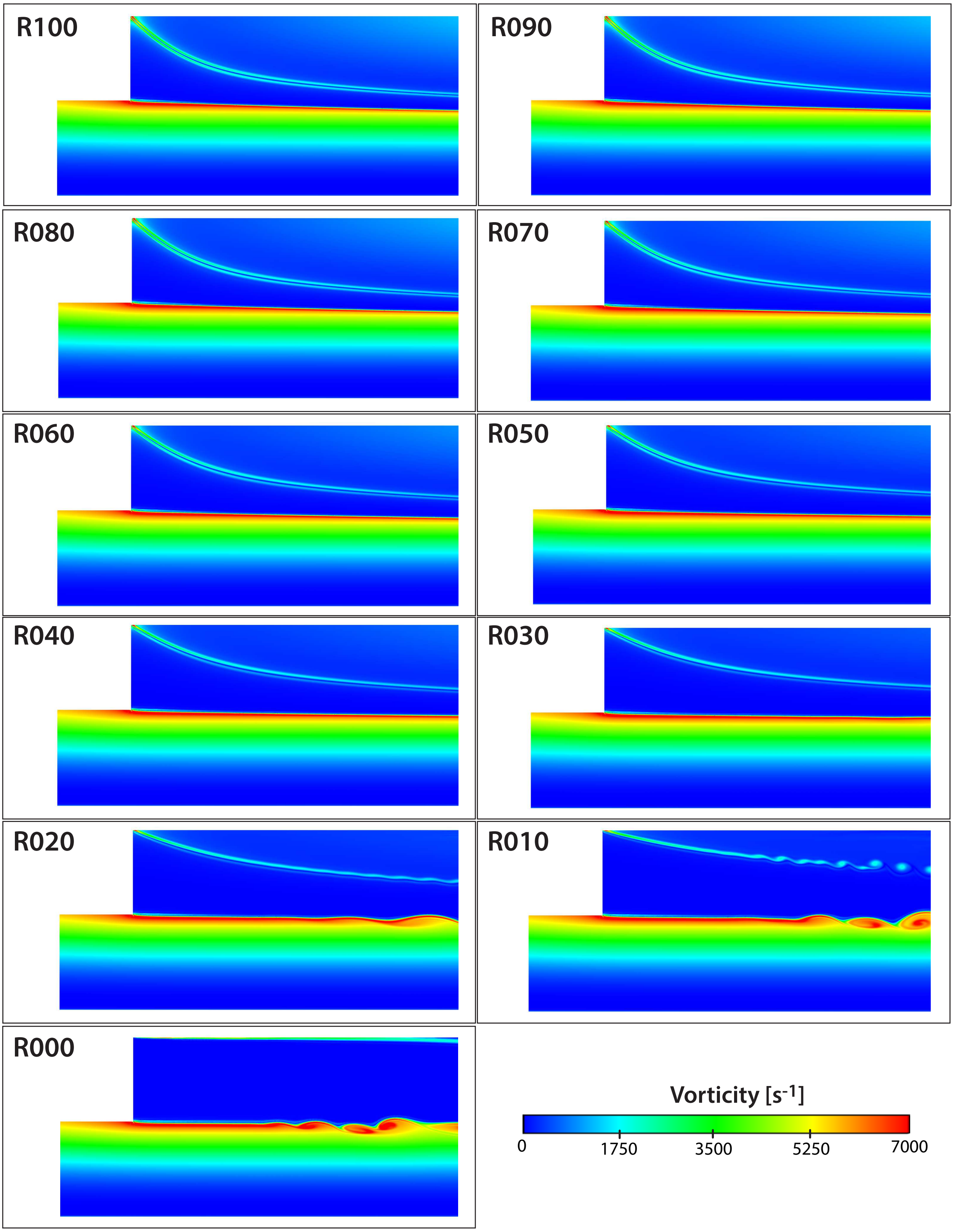

Figure 2. Instantaneous vorticity fields for the cases $R100$ to $R000$

Case name	Q_{P4} $[kg.m^{-2}.s^{-1}]$
R100	50.82
R090	45.74
R080	40.16
R070	35.14
R060	30.12
R050	25.10
R040	20.08
R030	15.06
R020	10.04
R010	5.02
R000	0.00

Table 2. Test case matrix with varying mass flow rate Q_{P4}.

shear layer when lateral blowing increases. Indeed, as shown in Fig. 2, vortices first appear at a blowing level of 20% of the nominal value (case *R020*). With higher blowing intensity, the mixing layer seems to be stable.
To measure the instability intensity, FFTs of axial velocity signals are performed at a probe P_0 located at the black cross symbolized in Fig. 1.
As shown in Fig. 3, the case *R030* corresponding to Fig. 3(c) is the first case where peaks are present in the FFT. The maximum amplitude in frequency increases when lateral blowing decreases as visualized for case *R020* in Fig. 3(d), whereas only noise is present for *R050* and *R040* respectively in Fig. 3(a) and (b).
These results clearly confirm that increasing the lateral blowing on the shear layer tends to stabilize the CVS instability. It should be noted that in this configuration, at nominal conditions corresponding to case $R100$, no CVS is observed.

The frequency of the instability is quite dependent on the blowing intensity, as shown in Fig. 4 where the maximum amplitude in frequency is plotted for the cases where an instability was present, namely cases *R030*, *R020*, *R010* and *R000*. The instability frequency increases from 520 Hz for 0% blowing (*R000*) to 760 Hz for 30% blowing (*R030*).

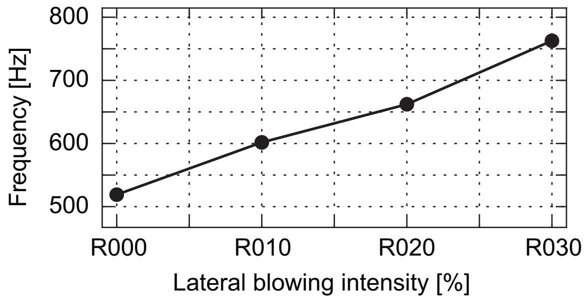

Figure 4. Instability frequency evolution with lateral blowing intensity.

5. LINEAR STABILITY ANALYSIS : CONCEPTS AND VALIDATION

Numerical simulations have highlighted the stabilization effect of lateral blowing on CVS in headwalls induced flows. However, unsteady simulations do not allow to clearly identify the regions of the flow or the triggering mechanisms that are generating this instability.
Physical insight into the causes of instability can be obtained by performing linear stability analysis of the time-averaged flow. This kind of analysis has already been proven useful in academic configurations like vortex shedding downstream a cylinder [27], parietal vortex shedding in solid rocket motors [9], [2], [14] as well as fuel injectors exhibiting

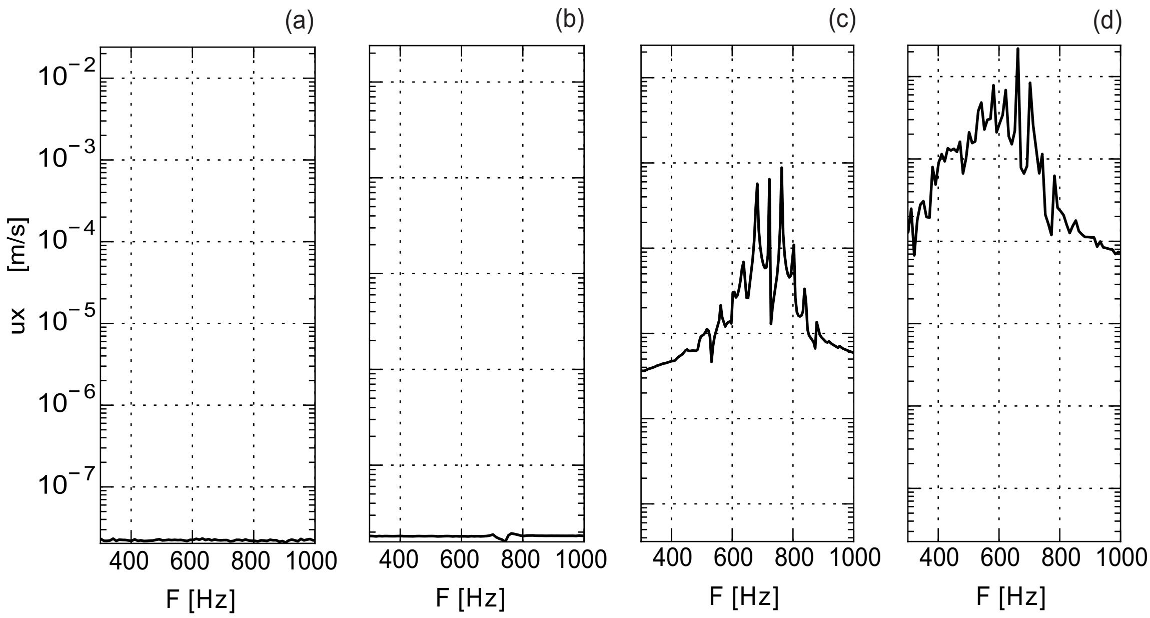

Figure 3. FFTs of axial velocity signals recorded at P_0 for cases (a): R050, (b): R040, (c): R030 and (d): R020

coherent structures in swirled jets [32], [26].

A local analysis formalism is used in this work, meaning that the local stability behaviour is computed at each axial position of the flow based on local time-averaged velocity profiles at the given axial position.

5.1. The linear stability theory and numerical methods

In this approach the Navier-Stokes equations are linearized around a steady axisymmetric base flow. Then, each quantity Q can be decomposed into a mean part $\bar{Q}$ also called the base flow and a fluctuating part q to be determined. For an axisymmetric and incompressible flow, the decomposed variables are defined by Eq. (1).

$$\begin{aligned}(U_x, U_r, U_\theta, P)(x, r, \theta) = &(\bar{U}_x, \bar{U}_r, \bar{U}_\theta, \bar{P})(x, r) + \\ &(u_x, u_r, u_\theta, p)(x, r, \theta, t)\end{aligned} \tag{1}$$

Following the parallel flow hypothesis, the base flow is assumed to only depend on the radial coordinate r. It should be noted that this hypothesis is not fully satisfied here since the geometry and the parietal injection imposed an axial dependence of the base flow, significant at the proximity of the corner, ignored here. However this assumption has been successfully used in the stability study of the VSP where good agreement between theoretical and experimental results are found [37], [23].

Fluctuating quantities q are formulated using normal mode decomposition given by Eq. (2).

$$q(x, r, \theta, t) = \hat{q}(r) e^{i(\alpha x + m\theta - \omega t)} \tag{2}$$

In Eq. (2) $\hat{q}$ is a complex function called amplitude function, m is an integer representing the azimuthal wave number and α and ω are generally complex numbers.

In the case of a convective instability like the one expected in the present mixing layer, using a spatial analysis formalism is more relevant and is the one chosen in this work. Therefore ω is a real number and $\alpha = \alpha_r + i\alpha_i$ is a complex value. In this work the azimuthal wave number m is set to zero since only axisymmetric modes are studied in agreement with the axisymmetric simulations presented above. Eq. (2) can then be rewritten in Eq. (3).

$$q(x, r, \theta, t) = \hat{q}(r) e^{-\alpha_i x} e^{i(\alpha_r x - \omega t)} \tag{3}$$

In Eq. (3) the second exponential term is of norm one and describes the wavy nature of the solution for the fluctuation, α_r being the wave number and ω the circular frequency, with $f = \omega/2\pi$ being the frequency itself. The first exponential in Eq. (3) is real and reflects the amplification or the attenuation of the perturbation with the distance x according to the sign of α_i and the propagation direction of the unstable mode.

The problem now is to determine the amplitude function $\hat{q}$ as well as the frequency and complex wave number α, so that perturbations given by Eq. (3) satisfy the linearized Navier-Stokes equations and boundary conditions. These conditions constitute the dispersion relation defined by Eq. (4). Except for very simple cases, this relation cannot be analytically determined and is solved numerically.

$$\mathcal{F}(\bar{Q}, \alpha, \omega, m) = 0 \tag{4}$$

After discretization the linearized equations can be transformed into a generalized eigenvalue problem as the one expressed in Eq. (5). X, defined by Eq. (6) is a vector holding unknowns $\hat{q}_j$ at each discretization point j.

$$A.X = \alpha.B.X \tag{5}$$

$$X = [\hat{u}_x, \hat{u}_r, \hat{u}_\theta, \hat{p}] \tag{6}$$

The linearized equations are associated to boundary conditions at the wall ($r = R_2$, Eq. (7)) and at the axis ($r = 0$, Eq. (8) with $m = 0$).

$$\hat{u}_x(R_2) = \hat{u}_r(R_2) = \hat{u}_\theta(R_2) = 0 \tag{7}$$

$$\frac{d\hat{u}_x}{dr}(0) = \hat{u}_r(0) = \hat{u}_\theta(0) = 0 \tag{8}$$

Several methods can be used to solve an eigenvalue problem but the one chosen is the spectral collocation method [8] which consists in decomposing the functions to discretize, here the amplitude functions, on a polynomial basis. The Tchebytchev polynomials are used associated to Gauss-Lobatto disctretization points. More details can be found in [8].

5.2. Validation

The linear stability solver described above has been validated for instance the Taylor-Culick flow, for which stability is nowadays well known and has been the subject of several publications, including [9, 10, 24, 23, 11, 6].

Tab. 3 presents the comparison of the eigenvalues of the three most amplified modes obtained with the solver to the reference values of [2].

	Reference results [2]		Solver results	
Mode	α_r	α_i	α_r	α_i
1	6.095	-1.078	6.095	-1.078
2	3.326	-0.109	3.326	-0.109
3	2.601	0.132	2.601	0.132

Table 3. Eigenvalues comparison of the three most amplified modes with reference values [2]

Results are equal, the difference being lower than 10^{-4}, which validates the solver.

6. STABILITY ANALYSIS OF AN UNSTABLE CASE

In this section the weakly unstable case $R030$ is analysed. The aim described above is to evaluate if the local stability analysis enables first to select the same instability frequencies as in the unsteady simulation and second to capture the spatial evolution of the selected mode.

6.1. Method of analysis

The following stability study is split into three parts.
In the first part, one axial position $x_0 = 0.04$ m away from the geometry corner is studied and the computed dispersion curve is compared to the FFT of the signal recorded at the same axial position x_0. The shape of the modulus $|\hat{u}_x(r)|$ and the phase $\varphi_{\hat{u}_x}(r)$ of the eigenfunction $\hat{u}_x(r)$ defined by Eq. (9) are also compared at the frequency instability with the one found by dynamic mode decomposition (DMD) analysis of the unsteady simulation solution [33].

$$\hat{u}_x(r) = |\hat{u}_x(r)| e^{i\varphi_{\hat{u}_x}(r)} \tag{9}$$

In the second part, dispersion curves are computed for several axial positions leading to the determination of the spatial amplification e^n of the perturbation at the instability frequency.
e^n is the term that modifies the amplitude of the axial velocity perturbation u_x as defined in Eq. (10) with $m = 0$ and $t = 0$.

$$u_x(x, r, t) = |\hat{u}_x(r)| e^n e^{i(\varphi_{\alpha_r} + \varphi_{\hat{u}_x}(r))} \tag{10}$$

n, called the n-factor represents the integration of $-\alpha_i$ over the upstream positions. The value of n at axial position x is defined by Eq. (11), x_0 being the first position studied.

$$n = \int_{x_0}^{x} -\alpha_i(\xi) d\xi \tag{11}$$

The axial evolution of e^n is directly compared to the axial evolution of the FFT magnitude given by the simulation results.
In the last part, by combining the modulus $|\hat{u}_x(r)|e^n$ and the phase $\varphi_{\alpha_r} + \varphi_{\hat{u}_x}(r)$, defined in Eq. (10), the 2D perturbation is reconstructed. φ_{α_r} is the phase introduced by the axial wave number α_r integrated over the previous positions as defined in Eq. (12).

$$\varphi_{\alpha_r} = \int_{x_0}^{x} \alpha_r(\xi) d\xi \tag{12}$$

The axial velocity perturbation reconstruction is finally compared to the simulation result.

6.2. Study at one axial position x_0

The first linear stability analysis is performed on mean velocity profiles at the axial position $x_0 = 0.04$m away from the geometry corner, represented by the black line on the vorticity field in Fig. 5.

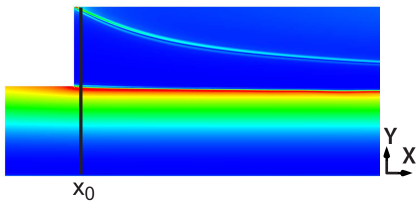

Figure 5. Location of the first stability analysis.

The mean velocity profiles and gradients at this position are plotted in Fig. 6.

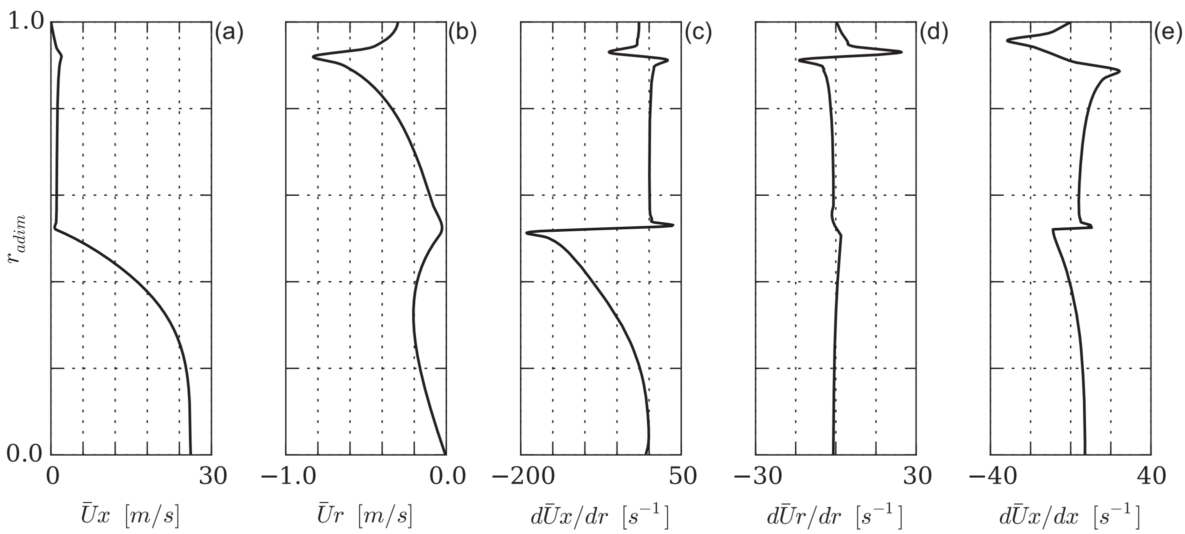

Figure 6. Mean velocity profiles and gradients at x=0.04m as a function of $r_{adim} = r/R_2$. (a),(b): axial and radial velocity profiles; (c),(d): axial and radial velocity gradients with respect to the radial coordinate, (e): axial velocity gradient with respect to the axial coordinate.

The radial coordinate is normalized by the radius $R_2 = 0.25$ m and the velocity profiles are normalized by the axial velocity on the axis $\bar{U}x_{r=0} = 267$ m/s at this position. This high axial velocity is linked to the high velocity injection chosen.
In Fig. 7 the FFT of the simulation signal at x_0 is compared to the computed evolution of the spatial amplification $-\alpha_i$ as a function of the perturbation frequency $f = \omega/2\pi$.

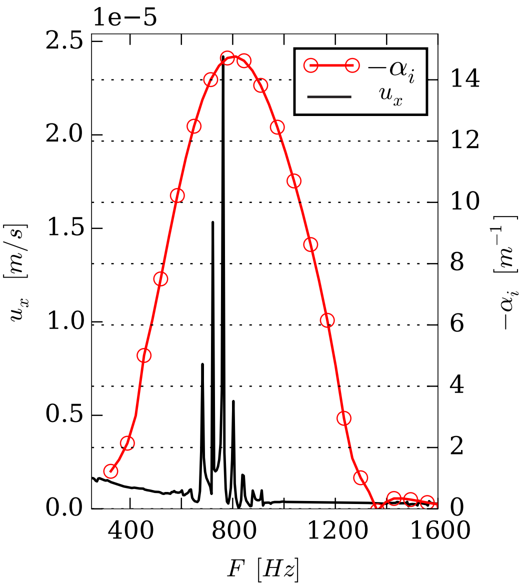

Figure 7. Comparison of the spatial amplification $-\alpha_i$ (red line with symbols) with the FFT of the unsteady simulation signal (black line without symbol) at x_0 as a function of frequency.

As shown on Fig. 7, the stability analysis captures well the frequency of the dominating mode at this position. The unstable frequency range is however larger in the stability analysis than in the unsteady simulation where few frequencies are present.
A DMD analysis [33] of the simulation results enables to compute the modulus and the phase of the mode at the instability frequency of 720 Hz. This modulus and phase can be compared to the ones found by the stability analysis for a perturbation at the same frequency. This comparison is shown in Fig. 8.(a) for the modulus and in Fig. 8.(b) for the phase. The amplitude of the modulus is scaled and the phase is shifted with a constant value to match the DMD results. As shown in Fig. 8 the stability analysis captures remarkably well the shape of the modulus and the phase of the visualized mode.

6.3. Amplification factor computation

The aim of this part is to evaluate the axial evolution of the perturbation amplitude, called the n-factor defined in Eq. 11. To do so, the dispersion curve is computed for several axial positions from $x_0 = 0.04$ m to $x_{18} = 0.40$ m with a step of $\Delta_x = 0.02$ m, as

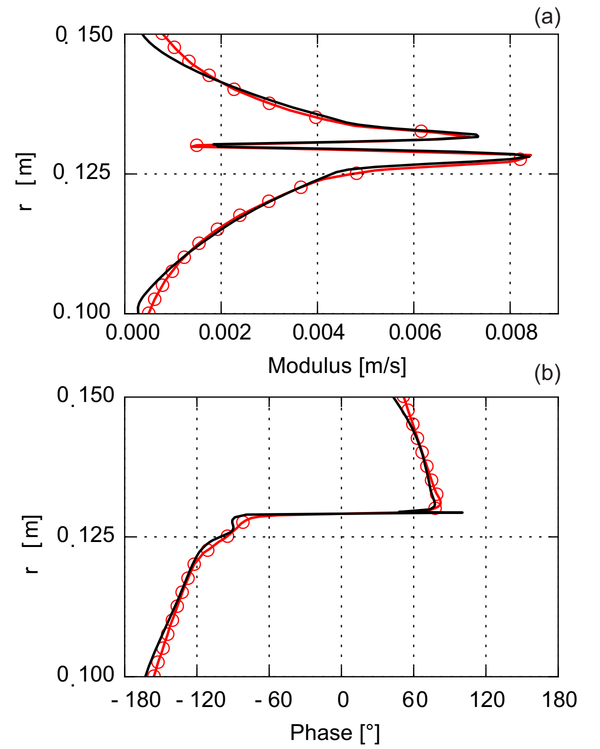

Figure 8. Comparison of the eigenvector modulus (a) and phase (b) between stability analysis (red line with symbols) and DMD of unsteady simulation results (black line without symbol) at x_0.

shown in Fig. 9.
Fig. 10.(a) shows all the dispersion curves computed and Fig. 10.(b) shows the axial evolution of e^n. As visualized in Fig. 10.(a), when going downstream the dispersion curve flattens and the most amplified frequency increases.

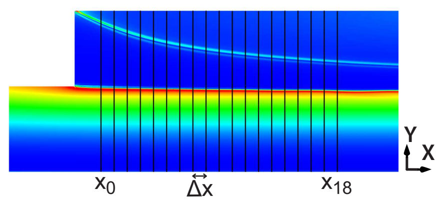

Figure 9. Location of the performed stability analysis.

This phenomenon is recovered in the evolution of the exponential of the n-factor plotted in Fig. 10.(b). The most amplified frequency is shifted from 720 Hz for the first position x_0 to 1060 Hz when the entire domain is considered (from x_0 to x_{18}).
This frequency shift is not visible in the unsteady simulation as shown on the FFT of signals at several axial positions plotted in Fig. 11.
The local stability analysis induced by the quasi-parallel approximation used may not be sufficient to properly captured the frequency selection mechanism. Indeed the corner in the geometry imposed a strong axial dependence of the mean flow at the proximity of the corner.

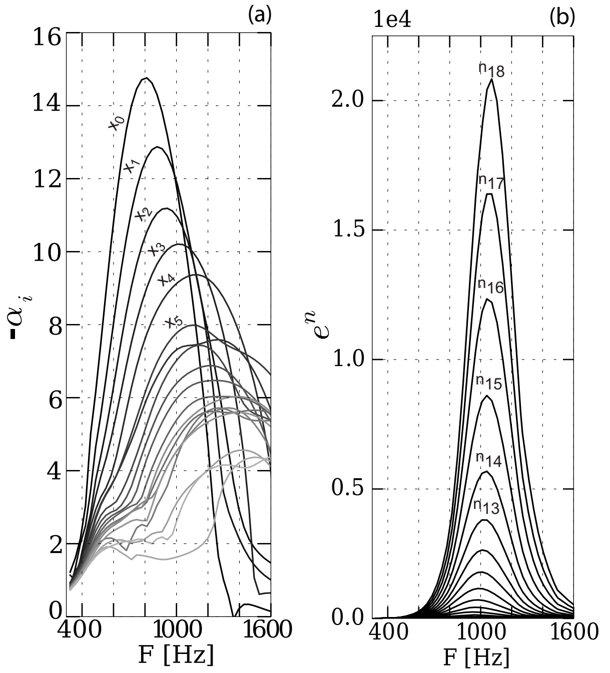

Figure 10. (a): Evolution of α_i for each axial position from x_0 to x_{18}. The lighter the color line the further the axial position. (b): Evolution of e^n when integration domain increases. Line n_X means integration from x_0 to x_X.

The quasi-parallel hypothesis can be then contested in this case. To outcome this limitation, a biglobal method with no hypothesis on the base flow could be used. This method outlined by [5] and applied to the solid rocket motor flow [13], [14], [15] tends to be more realistic than the local analysis even if in the case of the parietal vortex shedding instability the quasi-parallel flow assumption gives good results.

However, the amplitude evolution of the perturbation at the unstable frequencies are well captured by the local stability analysis as shown on Fig. 11, where the red symbols represent the values of $A_0.e^n$, A_0 being a constant fixed to match the FFT amplitude at the last position x_{18}.

6.4. Perturbation reconstruction

The objective of this part is to reconstruct the 2D field of axial perturbation $u_x(x,r,t)$ at the mode frequency of 720 Hz.

The modulus evolution $A_0|\hat{u}_x(r)|e^n$ is plotted in Fig. 12.(a). The shape and the amplitude evolution are perfectly captured by the linear stability analysis.

The phase evolution $\varphi(r) = \varphi_{\alpha_r} + \varphi_{\hat{u}_x}(r)$ is plotted in Fig. 12.(b). After normalization of the phase eigenfunction $\varphi_{\hat{u}_x}(r)$, the phase of the perturbation $\varphi(r)$ is shifted by the same offset value fixed so that phase matches at the last position x_{18} as visualized on Fig. 12.(6b).

As shown in Fig. 12.(b) the shape of computed phase is coherent with the one of the simulation even if a deviation progressively grows.

Finally the full 2D reconstruction of the axial perturbation $u_x(x,r,t)$ is performed and compared to the axial velocity perturbation of the simulation result.

As shown on Fig. 13, the reconstructed perturbation is very close to the one of the simulation.

Linear stability thus is able to predict the shape and the space-time evolution of the perturbation with good accuracy.

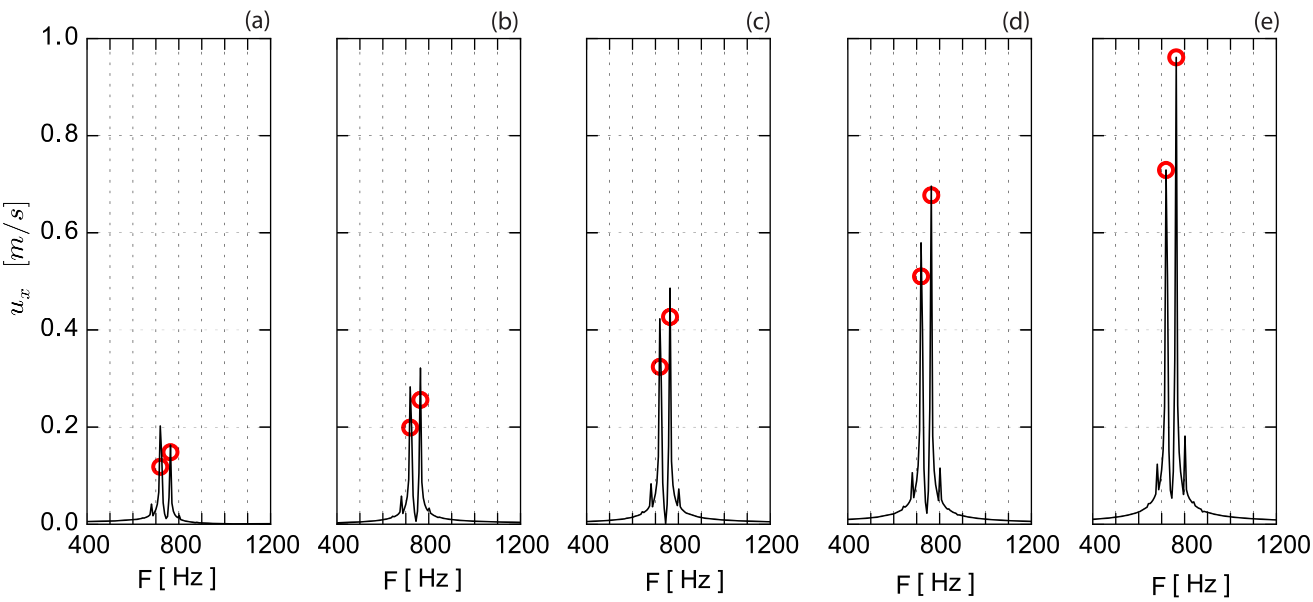

Figure 11. Comparison of the value of $A_0.e^n$ at the two maximum amplitude frequencies (red symbols) with the FFT on simulation velocity signal. (black line without symbol). (a),(b),(c),(d),(e): respectively at x_{10}, x_{12}, x_{14}, x_{16}, x_{18}.

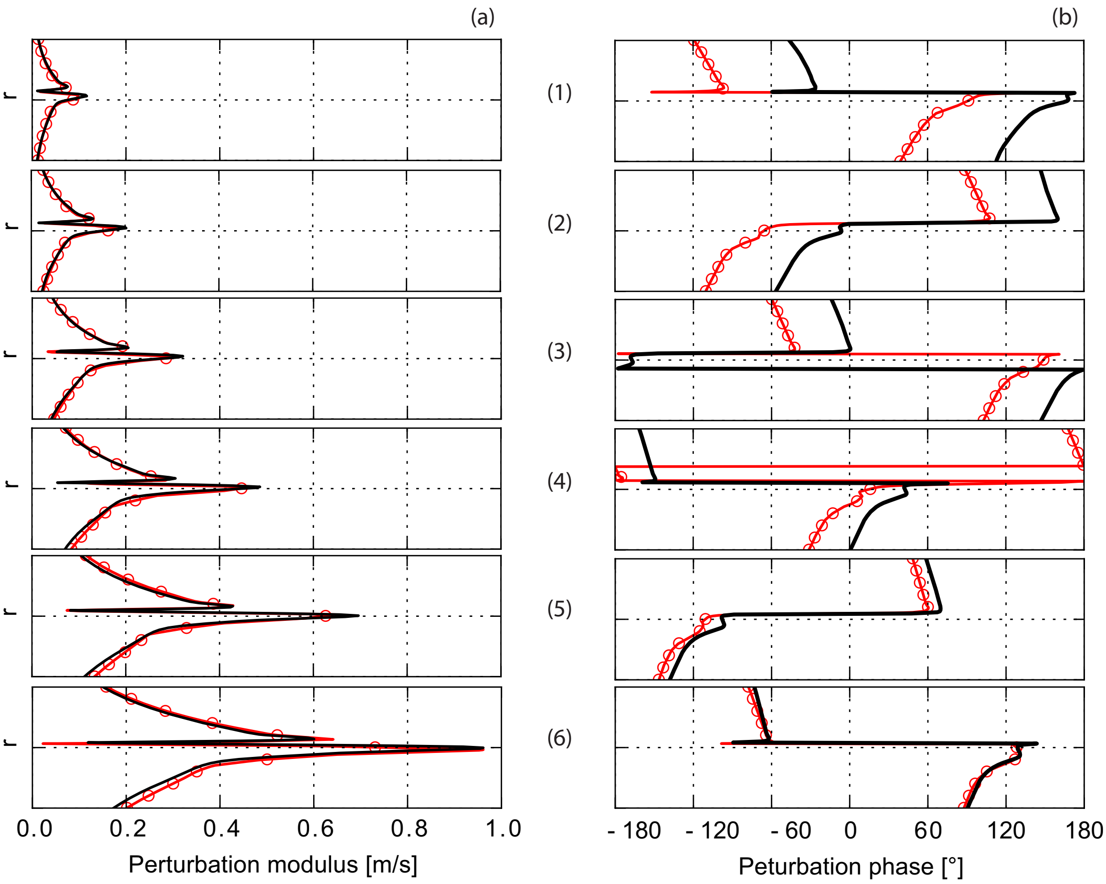

Figure 12. Comparison of stability analysis (red line with symbols) and DMD of simulation results (black line without symbol). (a) comparison of the modulus and (b) the phase of the axial perturbation at several axial positions, (1),(2),(3),(4),(5),(6): respectively at x_8, x_{10}, x_{12}, x_{14}, x_{16}, x_{18}.

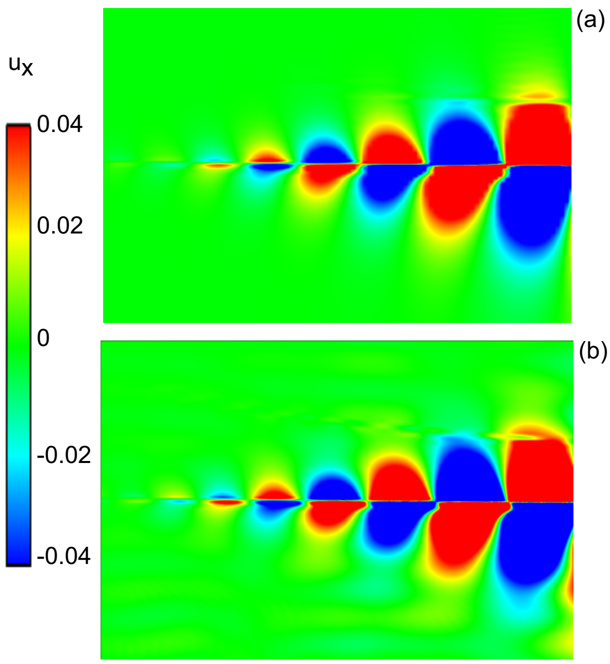

Figure 13. Comparison of the reconstructed axial velocity perturbation from linear stability (a) and the field of the axial velocity perturbation in the simulation (b).

7. STABILITY STUDY OF A STABLE CASE

The same analysis is applied to the perfectly stable case $R080$. Since the unsteady simulation exhibits no unstable frequency, no amplified frequencies should appear in the linear stability analysis.
However, weakly amplified frequencies are found as illustrated by the n-factor evolution plotted on Fig. 14.
This amplification factor is smaller by a factor 10 compared to the one of the case $R030$ plotted on Fig. 10.(b). This means that the perturbation will be much less spatially amplified than in the previous unstable case and may not be sufficient to sustain an instability in the simulation.
The difference in the stability prediction between the simulation and the local linear stability analysis could also be an outcome of the quasi parallel stability analysis limits.
However this analysis enables to capture the tendency of stabilisation of the CVS by lateral blowing.

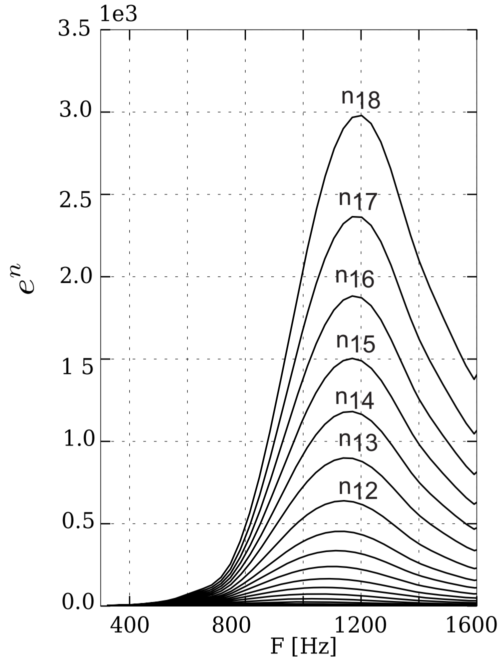

Figure 14. Evolution of e^n when integration domain increases. Line n_X means integration from x_0 to x_X.

8. CONCLUSIONS

Parametric unsteady simulations on an academic case reproducing the CVS in solid rocket motors have shown that lateral blowing has a strong impact on the stability of the mixing layer. Increasing blowing intensity tends to attenuate and even suppress the CVS. This phenomenon has been qualitatively observed on instantaneous vorticity fields and quantitatively measured by axial velocity signal analysis.

A local linear stability analysis was performed to identify the triggering mechanisms of this instability and confirm that the fluctuations are induced by an intrinsic hydrodynamic instability of the shear layer.

An unstable case is first studied and results show that the local formalism induced by the quasi-parallel approximation may not be sufficient to reproduce the frequency selection mechanism. However, excellent results are obtained for the prediction of the 2D axial velocity perturbation at the correct frequency.

Stability analysis is finally performed on a stable case and unlike the simulations, weakly amplified frequencies are found. Nevertheless, the tendency of stabilization by the lateral blowing found by the simulation is recovered.

Even if the analysis reveals some limits, with this powerful method the stabilization of the shear layer with its principal characteristics obtained in the unsteady simulations are recovered.

ACKNOWLEDGEMENTS

This work has been performed in the framework of a thesis supported by Herakles and performed at CERFACS. Authors thank T. Pevergne, F. Godfroy and J. Richard from Herakles for the support they have brought to this study.

9. REFERENCES

1. CERFACS and AVBP websites. `http://cerfacs.fr/en/`, `http://www.cerfacs.fr/avbp7x/`.

2. E. M. Abu-Irshaid, J. Majdalani, and G. Casalis. Hydrodynamic stability of rockets with headwall injection. *Physics of Fluids*, 19(2):024101, 2007.

3. G. Avalon and T. Josset. Cold gas experiments applied to the understanding of aeroacoustic phenomena inside solid propellant boosters. *AIAA*, 2006.

4. S. Ballereau, F. Godfroy, S. Gallier, and O. Orlandi. Evaluation method of thrust oscillations in large SRM application to segmented SRM's. *AIAA paper*, 2011.

5. J. W. Batterson and J. Majdalani. Biglobal instability of the bidirectional vortex. Part 1: Formulation. *AIAA Conference*, 2011.

6. G. Boyer. *Etude de stabilité et simulation numérique de l'écoulement interne des moteurs à propergol solide simplifiés*. PhD thesis, Institut Supérieur de l'Aéronautique et de l'Espace (ISAE), 2012.

7. R. Brown, R. Dunlap, S. Young, and R. Waugh. Vortex Shedding as a Source of Acoustic Energy in Segmented Solid Rockets. *Journal of Spacecraft and Rockets*, 18(4):312–319, July 1981.

8. C. Canuto. *Spectral Methods in Fluid Dynamics*. Springer Verlag, 1988.

9. G. Casalis, G. Avalon, and J.-P. Pineau. Spatial instability of planar channel flow with fluid injection through porous walls. *Physics of Fluids*, 10(1):2558–2568, Oct. 1998.

10. G. Casalis and F. Vuillot. Motor Flow Instabilities-Part 2. Intrinsic Linear Stability of the Flow Induced by Wall Injection. In *RTO-AVT VKI Special Course on Internal aerodynamics in solid rocket propulsion, RTO-EN-023*. 2004.

11. F. Chedevergne. *Instabilités intrinsèques des moteurs à propulsion solide.* PhD thesis, ENSAE, 2007.

12. F. Chedevergne and G. Casalis. Thrust oscillations in reduced scale solid rocket motors, part II: A new theoretical approach. *AIAA Conference*, 2005.

13. F. Chedevergne and G. Casalis. Detailed analysis of the thrust oscillations in reduced scale solid rocket motors. *AIAA paper*, 2006.

14. F. Chedevergne, G. Casalis, and T. Féraille. Biglobal linear stability analysis of the flow induced by wall injection. *Physics of Fluids*, 18(1):014103, 2006.

15. F. Chedevergne, G. Casalis, and J. Majdalani. Direct numerical simulation and biglobal stability investigations of the gaseous motion in solid rocket motors. *Journal of Fluid Mechanics*, 706:190–218, July 2012.

16. O. Colin and M. Rudgyard. Development of high-order taylor–galerkin schemes for les. *Journal of Computational Physics*, 162(2):338–371, 2000.

17. F. Culick. Rotational axisymmetric mean flow and damping of acoustic waves in asolid propellant rocket. *AIAA Journal*, 4(8):1462–1464, 1966.

18. P. Drazin and W. Reid. Hydrodynamic stability. *Cambridge University Press*, 1981.

19. R. Dunlap, A. M. Blackner, R. C. Waugh, R. S. Brown, and P. G. Willoughby. Internal flow field studies in a simulated cylindrical port rocket chamber. *Journal of propulsion and power*, 6(6):690–704, Nov. 1990.

20. Y. Fabignon, J. Dupays, G. Avalon, F. Vuillot, N. Lupoglazoff, G. Casalis, and M. Prevost. Instabilities and pressure oscillations in solid rocket motors. *Aerospace Science and Technology*, 7:191–200, 2003.

21. G. A. Flandro and J. Majdalani. Aeroacoustic Instability in Rockets. *AIAA Journal*, 41:485–497, Mar. 2003.

22. J. Griffond and G. Casalis. On the dependence on the formulation of some nonparallel stability approaches applied to the Taylor flow. *Physics of Fluids*, 12(2):466, 2000.

23. J. Griffond and G. Casalis. On the nonparallel stability of the injection induced two-dimensional Taylor flow. *Physics of Fluids*, 13(6):1635, 2001.

24. J. Griffond, G. Casalis, and J.-P. Pineau. Spatial instability of flow in a semiinfinite cylinder with fluid injection through its porous walls. *European Journal of Mechanics - B/Fluids*, 19(1):69–87, 2000.

25. P. Huerre, G. Batchelor, H. Moffatt, and M. Worster. Open shear flow instabilities. *Perspectives in Fluid Dynamics*, pages 159–229, 2000.

26. M. P. Juniper. Absolute and convective instability in gas turbine fuel injectors. pages 1–10, Feb. 2012.

27. W. Koch. Local instability characteristics and frequency determination of self-excited wake flows. *Journal of Sound and Vibration*, 99(1):53–83, Mar. 1985.

28. J. Majdalani and T. Saad. Internal Flows Driven by Wall-Normal Injection. In H. W. Oh, editor, *Advanced Fluid Dynamics*. InTech, Mar. 2012.

29. J. Majdalani and W. Van Moorhem. Multiple scales solution to the acoustic boundary layer in solid rocket motors. *Journal of propulsion and power*, 13(2):186–193, 1997.

30. A. Michalke. On the inviscid instability of the hyperbolictangent velocity profile. *Journal of Fluid Mechanics*, 1964.

31. A. Michalke. On spatially growing disturbances in an inviscid shear layer. *Journal of Fluid Mechanics*, 1965.

32. K. Oberleithner et al. Three-dimensional coherent structures in a swirling jet undergoing vortex breakdown: stability analysis and empirical mode construction. *Journal of Fluid Mechanics*, 679:383–414, May 2011.

33. P. J. Schmid. Dynamic mode decomposition of numerical and experimental data. *Journal of Fluid Mechanics*, 656:5–28, July 2010.

34. P. J. Schmid and D. S. Henningson. *Stability and Transition in Shear Flows*. Springer Verlag, Dec. 2001.

35. G. Taylor. Fluid flow in regions bounded by porous surfaces. *Proceedings of the Royal Society of London. Series A. Mathematical and Physical Sciences*, 234(1199):456–475, 1956.

36. B. Ugurtas, G. Avalon, N. Lupoglazoff, and F. vuillot. Numerical computations and visualization tests of the flow inside a cold gas simulation with characterization of a parietal vortex shedding. *AIAA*, 2000.

37. B. Ugurtas, G. Avalon, N. Lupoglazoff, and F. vuillot. Stability and acoustic resonance of internal flows generated by side injection. *Progress in astronautics and aeronautics*, 2000.

38. V. N. Varapaev and V. I. Yagodkin. Flow stability in a channel with porous walls. *Fluid Dynamics*, 1969.

39. F. Vuillot. Vortex-shedding phenomena in solid rocket motors. *Journal of propulsion and power*, 11(4):626–639, July 1995.